Online collaborative estimation technology for SOC and SOH of frequency regulation of a lead-carbon battery in a power system with a high proportion of renewable energy

Hongchun Shu, *Member*, *IEEE*, Wenlong Li, Guangxue Wang, *Student Member*, *IEEE*, Yiming Han, *Member*, *IEEE*, Jiannan Li, and Yutao Tang, *Student Member*, *IEEE*

***Abstract*—In this paper, a collaborative online algorithm is proposed to estimate the state of charge (SOC) and state of health (SOH) of lead-carbon batteries that participate in frequency regulation of a power system with a high proportion of renewable energy. The algorithm addresses the inaccurate estimation of energy storage battery states caused by continuous and alternating charging and discharging over a short period. Analysis of lead-carbon battery chemistry and materials reveals that the resistance of the diaphragm is the most influential factor in battery aging. In addition, the hysteresis characteristics of an energy storage battery vary significantly between the charging and discharging stages. A second-order RC equivalent circuit model is proposed that considers the contact and diaphragm resistances, and hysteresis characteristics. Based on this, models for constant current charging interaction, constant voltage charging interaction, and dynamic discharging interaction are developed. The adaptive forgetting factor recursive least square (AFF-RLS) method is used to identify the parameters of the interactive models. Then an interactive multiple model with the embedded unscented Kalman filter (UKF) is used to estimate the SOC of the energy storage battery. The membrane and contact resistances identified by the interactive multi-model (IMM) are used to estimate the SOH, and online collaborative optimization of the SOC and SOH is achieved. The error of the proposed SOC estimation method is experimentally verified to be within 2%, which is less than 5% of the standard value, and the error of SOH estimation is within 0.5%, demonstrating the high accuracy of the proposed method.**

***Index Terms*—Battery state of charge, battery health status, interactive multi-model, parameter identification.**

I. Introduction

Renewable energy is the basic direction for green and low-carbon power system transformation [1]–[3]. Renewable energy power generation based on large-scale wind and photovoltaic power exhibits intermittence and volatility. A high proportion of renewable energy grid connection will present significant challenges to the power system's power balance and frequency stability. Electrochemical energy storage is capable of regulating the frequency and voltage of the power system and ensuring its safe and stable operation. This is achieved because of its fast response, strong short-term power throughput, high control accuracy, two-way regulation, and other characteristics [4]–[6].

Reference [6] comprehensively examines the state of charge (SOC) of the energy storage battery in the frequency regulation of a power system. It introduces a feedback coefficient to adjust the output of the battery energy storage system, thereby preventing the overcharging or over-discharging of the battery and enhancing the primary frequency regulation effect. It also increases the service life of the battery to a certain extent.

SOC and state of health (SOH) are the two most important battery parameters. The battery SOC is defined as the ratio between the remaining power of the battery under a certain discharge rate and the rated capacity under the same condition, while SOH is defined as a parameter that represents the ability of the battery to meet the established performance indicators in its current condition [7], [8]. The accurate estimation of SOC and SOH can enable the adoption of scientific and efficient control strategies by the battery management system (BMS), extend battery service life, and improve battery utilization [9].

Here we offer a literature review of SOC and SOH estimation. References [10], [11] use the ampere-hour integration method and its improved version for SOC estimation. This method is convenient, but current er-

Received: March 30, 2023
Accepted: October 12, 2023
Published Online: January 1, 2024
Guangxue Wang (corresponding author) is with the State Key Laboratory Collaborative Innovation Center for Smart Grid Fault Detection, Protection and Control Jointly, Kunming University of Science and Technology, Kunming 650000, China (e-mail: km_wgx@163.com).
DOI: 10.23919/PCMP.2023.000232

rors have a significant impact on estimation accuracy while it depends heavily on the initial SOC (SOC0). Moreover, long-term estimation errors will accumulate large errors. In [12], [13] the open-circuit voltage method is used. This has a fast calculation time. However, the open-circuit voltage cannot be obtained in a short period of time. A neural network method is used in [14], [15] to estimate the SOC. Although this method does not require a battery physical model, massive experimental data modeling is needed. References [16], [17] use artificial intelligence algorithms to estimate SOC and SOH, and while the proposed method has strong universality, it also relies on massive data for modeling. In [18]–[20], the Kalman filter and its improved version are used for SOC estimation, where its one-step prediction and one-step correction can enable real-time and accurate online SOC estimation. Consequently, this method is currently the most commonly used SOC estimation method.

The SOC and SOH estimations of batteries described in the above literature are mainly applicable to lithium-ion batteries in electric vehicles. There is no continuous alternating process of charging and discharging at the second or minute level over a short time scale. However, when energy storage batteries play a significant role in frequency modulation in new energy power systems, they must operate alternately during charging and discharging over such a short time scale. This will place greater demands on the SOC estimation of batteries, rendering the above methods inapplicable.

Given the preceding analysis, an online collaborative estimation algorithm for SOC and SOH of frequency-regulating lead-carbon batteries in power systems with a high proportion of renewable energy is proposed. The interactive models of constant current and voltage charging, and dynamic discharge are developed using the second-order RC equivalent circuit model, which considers the contact and diaphragm resistances, and hysteresis characteristics. The parameters of the three models are identified by the adaptive forgetting factor recursive least square (AFF-RLS) methods. Subsequently, the SOC is estimated by an interactive multi-model (IMM) algorithm with embedded unscented Kalman filter (UKF), while the battery SOH is estimated using the identified battery diaphragm and contact resistances. Experiments with the measured data verify that the errors of SOC and SOH estimated by the proposed method are within 2% and 0.5%, respectively, demonstrating the high estimation accuracy.

II. Establishment of Lead-carbon Battery Model

The lead-carbon battery is considered to be a super battery [21], and its operating principle is shown in Fig. 1. The high conductivity and dispersion of lead-based materials in the carbon materials increase the battery's power output. The carbon materials of the negative and positive plates form an asymmetric capacitor to provide double-layer capacitance, which can reduce battery damage caused by high rate or pulse charging and discharging [22], [23]. Because of their high safety, low cost, and simple regeneration, lead-carbon batteries will become one of the main choices for large-scale energy storage [24].

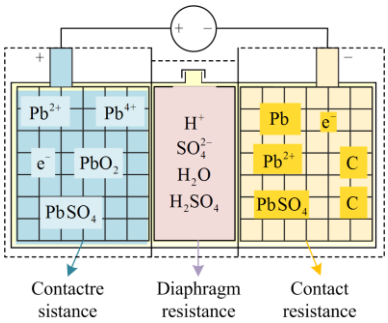

Fig. 1. Schematic diagram of lead-carbon battery.

Figure 1 shows that carbon does not participate in the chemical reaction. Therefore, the chemical reaction equation is the same as that of the lead-acid battery. The total reaction equation is shown in (1), while as its positive and negative chemical reactions are carried out separately and simultaneously, the negative and positive reactions are shown respectively in (2) and (3).

$$Pb + PbO_2 + 2H_2SO_4 \underset{\text{charge}}{\overset{\text{discharge}}{\rightleftharpoons}} 2PbSO_4 + 2H_2O \quad (1)$$

$$Pb + H_2SO_4 - 2e^- \underset{\text{charge}}{\overset{\text{discharge}}{\rightleftharpoons}} PbSO_4 + 2H^+ \quad (2)$$

$$PbO_2 + H_2SO_4 + 2H^+ + 2e^- \underset{\text{charge}}{\overset{\text{discharge}}{\rightleftharpoons}} PbSO_4 + 2H_2O \quad (3)$$

During the discharging process of the negative electrode, lead loses its electrons and is oxidized to divalent lead (Pb^{2+}). Subsequently, it reacts with sulfuric acid to form lead sulfate particles. During charging, the lead ions in lead sulfate particles are reduced to lead, and sulfuric acid is precipitated. During the discharge of the positive electrode, the tetravalent lead (Pb^{4+}) in lead dioxide is reduced to divalent lead (Pb^{2+}), which then reacts with sulfuric acid to form lead sulfate crystal. During the charging process, the divalent lead in lead sulfate is oxidized to tetravalent lead, producing lead dioxide and precipitating sulfuric acid. The total reaction equation reveals that the reaction of 1 mol PbO_2, 1 mol Pb, and 2 mol H_2SO_4 can theoretically release 2 F (2×26.80 Ah). However, the actual amount of electricity released by the lead-carbon battery does not exceed 50%–60% of the theoretical value.

The internal resistance of lead-carbon batteries is composed of ohmic and polarization resistance. The ohmic internal resistance consists of contact and dia-

phragm resistances. The contact resistance is mainly composed of metal or alloy, compound and contact resistances. Diaphragm resistance is mainly affected by the diaphragm material and thickness, electrolyte concentration, and battery height, and is the main factor that influences battery aging. During the process of an electrochemical reaction, the internal polarization resistance can also be divided into concentration and activation polarization resistances. The former reflects the effect of the lead sulfate layer on the diffusion rate of hydrogen ion (H^+) and sulfate ion (SO_4^{2-}) in sulfuric acid electrolyte relative to the electrode plate, while the latter reflects the effect of the lead sulfate layer on the active substance and sulfuric acid reaction area.

The relationship curves between open-circuit voltage and SOC of a lead-carbon battery obtained after several charge-discharge experiments are shown in Fig. 2.

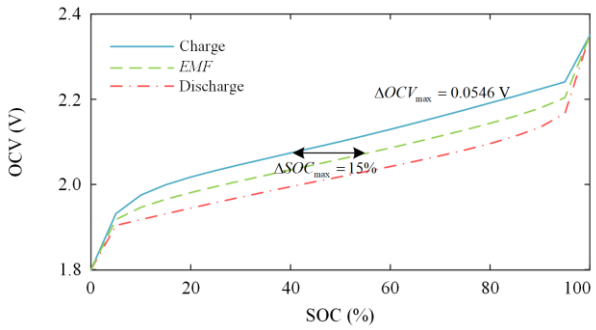

Fig. 2. Hysteresis characteristic voltage curve of lead-carbon battery.

It can be seen from Fig. 2 that the discrepancy between the open-circuit voltage when charging and discharging can reach 0.054 6 V under the same SOC, while the difference between SOC during charging and discharging under the same open-circuit voltage is as high as 15%. Therefore, the different hysteresis characteristics of charging and discharging must be considered during the process of modeling and parameter identification of the batteries.

Based on the above analysis, a lead-carbon battery equivalent circuit model is proposed as shown in Fig. 3, considering the contact and diaphragm resistances, and hysteresis characteristics. In Fig. 3, *EMF* represents the balanced electromotive force; u_h represents the hysteresis voltage; R_j represents the contact internal resistance; R_d represents the diaphragm resistance; R_1 and C_1 represent the concentration polarization resistance and capacitance respectively; R_2 and C_2 represent the activation polarization resistance and capacitance respectively; U_1 and u_2 represent the concentration and activation polarization voltages respectively. Unlike the conventional second-order model, the proposed model can account for the change in the contact and diaphragm resistances, as well as the hysteresis characteristics of the lead-carbon battery. It offers a clear physical interpretation of resistance and accurate parameter identification.

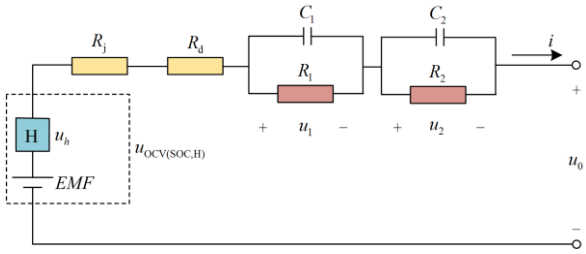

Fig. 3. Improved equivalent circuit model.

According to Kirchhoff's law, the equivalent circuit model shown in Fig. 3 can be established as:

$$\begin{cases} \dfrac{\mathrm{d}u_1}{\mathrm{d}t} = -\dfrac{u_1(t)}{R_1(t)C_1(t)} + \dfrac{1}{C_1(t)}i(t) \\ \dfrac{\mathrm{d}u_2}{\mathrm{d}t} = -\dfrac{u_2(t)}{R_2(t)C_2(t)} + \dfrac{1}{C_2(t)}i(t) \\ u_0(t) = u_{\mathrm{OCV(SOC,H)}}(t) - i(t)R_j(t) - \\ \qquad i(t)R_d(t) - u_1(t) - u_2(t) \end{cases} \tag{4}$$

where u_1 and u_2 are the concentration and activation polarization voltages, respectively. u_0 is the battery terminal voltage, $u_{\mathrm{OCV(SOC,H)}}$ is the open circuit voltage considering hysteresis characteristics and SOC values, i is the working current of the battery.

The hysteresis voltage u_h and balance potential *EMF* are calculated as:

$$\begin{cases} \text{Charging}: u_{\mathrm{h\_c}} = \eta(u_c - u_d) \\ \text{Discharging}: u_{\mathrm{h\_d}} = (1-\eta)(u_c - u_d) \\ EMF = \eta u_c + (1-\eta)u_d \end{cases} \tag{5}$$

where the value of η is between 0.5 to 1; $u_{\mathrm{h\_c}}$ and $u_{\mathrm{h\_d}}$ are the battery equilibrium terminal voltages when charging and discharging considering hysteresis characteristics, respectively; u_c and u_d are the battery equilibrium terminal voltages when charging and discharging, respectively.

The open-circuit voltage fitting is performed using the measured data of constant current and voltage charging, and then constant current discharging. The open-circuit voltage fitted by the conventional second-order RC model and the charge-discharge open-circuit voltage considering the hysteresis characteristics of the battery are shown in Fig. 4. The conventional second-order RC model uses the open-circuit voltage as the equilibrium potential voltage. This means that the inflection point of the open circuit voltages at the end of battery charging and at the beginning of discharge are essentially the same, consistent with the equilibrium potential *EMF* shown in Fig. 2.

This paper proposes an improved second-order RC model that takes into account the hysteresis characteristics of the battery. The inflection point voltage of the open-circuit voltage at the initial discharge stage is significantly lower than that at the end of charging. This is consistent with the charging and discharging open-circuit voltage experiment considering hysteresis characteristics shown in Fig. 2. Therefore, the model proposed in this paper is more in line with the actual state of lead-carbon batteries than the conventional method.

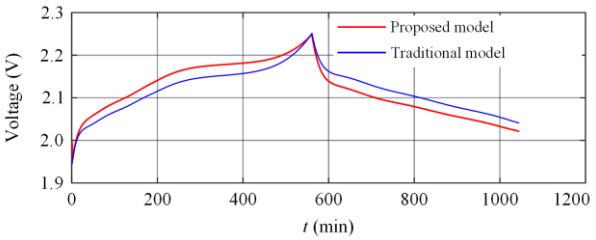

Fig. 4. Comparison of open circuit voltage between traditional and improved second-order models.

III. Interaction Model and Parameter Identification

Generally, rapid and uncontrolled charging will result in the electrolytic water producing a large amount of gas and the battery's temperature rising rapidly. Consequently, the battery's capacity degrades rapidly, and its service life is also drastically reduced. The cell voltage of 2.4 V can fluctuate suddenly in electrolytic water. The reaction of electrolytic water is very weak when the voltage is below 2.4 V, but when the voltage exceeds 2.4 V, electrolytic water will undergo an intense reaction.

Constant current charging is adopted when the voltage of a single battery is below 2.4 V. At this time, the weak electrolytic water capacity of the battery can be basically ignored. The charging reception capacity is the strongest and is almost equal to 100%. The generated resistance heat, energy loss, and polarization are not significant, and the corresponding SOC of the battery is about 70%. When the voltage reaches 2.4 V, the charging method changes to constant voltage charging, which shortens the charging time and alleviates the reaction of electrolytic water. When the voltage is higher than 2.5 V, the battery almost only conducts the reaction of electrolytic water. This results in the water loss of absorbent glass mat (AGM), and the ohmic resistance of the diaphragm increases. Furthermore, the concentration of sulfuric acid increases, which has two implications: 1) It corrodes the grid; and 2) It increases the potential difference and causes an increase in the degree of self-discharge. The battery is discharged according to the actual dynamic conditions. Based on this phenomenon, the models for constant current charging interaction, constant voltage charging interaction, and dynamic discharge interaction are established.

The model parameters of the three interactive models established above are identified using a real-time online parameter identification method. This method is known as AFF-RLS, whose derivation formula is given as:

$$\begin{cases} \lambda(g+1)=1-\dfrac{\mathrm{e}^2(g+1)}{(1+\varphi(g-l)\boldsymbol{P}(g)\varphi^{\mathrm{T}}(g-l))\times r} \\ \theta_{g+1}=\theta_g+\boldsymbol{K}(g+1)(y(g+1)-\varphi^{\mathrm{T}}(g+1)\theta_g) \\ \boldsymbol{K}(g+1)=\boldsymbol{P}(g)\varphi(g+1)(\lambda(g+1)+ \\ \qquad \varphi^{\mathrm{T}}(g+1)\boldsymbol{P}(g)\varphi(g+1))^{-1} \\ \boldsymbol{P}(g+1)=\dfrac{1}{\lambda(g+1)}(\boldsymbol{E}-\boldsymbol{K}(g+1)\varphi^{\mathrm{T}}(g+1))\boldsymbol{P}(g) \end{cases} \tag{6}$$

where λ is the adaptive forgetting factor; l and r are the adjustment coefficients; $e^2(g+1)$ is the square value of the estimation error; θ_g is the input of the parameter identification system; $\varphi^{\mathrm{T}}(g+1)\theta_g$ is the system observation value at time $g+1$; $y(g+1)$ is the real feedback value of the system at time $g+1$; $\boldsymbol{K}(g+1)$ is the system gain; φ is the measurement data; $\boldsymbol{E}$ is the identity matrix of the same type; and $\boldsymbol{P}(g+1)$ is the system covariance matrix.

During parameter identification, R_{j} is the contact internal resistance that can be regarded as a fixed value. Using an internal resistance tester, the value of R_{j} for the lead-carbon battery is measured as 1.36 mΩ. R_{d} is the diaphragm resistance, and as the battery ages, R_{d} shows an increasing trend. When it increases to twice of the value of that when the battery was new, it is considered that the battery has reached its end of life.

IV. Proposed SOC and SOH Estimation

A. Improved IMM-UKF Algorithm

The main idea of IMM is to fuse several different models, with each model filtered simultaneously and the transfer probabilities between models determined by the Markov chain (MC) probability transfer matrix [25], [26]. The untraced Kalman filter adds the untraced transform (UT) to the Kalman filter (KF) in order to consider the nonlinearity that exists for the transfer problem of probability density mean and covariance. Thus, the untraced Kalman filter is accurate for the non-linear battery estimation problem [27].

An interactive multi-model is mainly applied to the localization and tracking of maneuvering targets such as ships and vehicles. In these applications, only state quantities are used as inputs, with no interaction with external observations. However, the SOC and SOH estimations should consider the voltage and current measurements. Therefore, to meet this requirement, an

enhanced IMM algorithm is proposed that simultaneously considers state quantities, voltage, and current using a UKF. Figure 5 shows its flowchart.

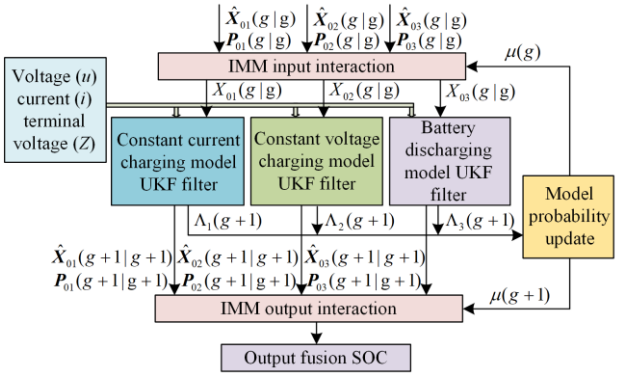

Fig. 5. Improved IMM-UKF algorithm flowchart.

B. SOC Estimation Driven by Model and Measured Data

Different voltage and current data correspond to different battery parameters. Different interactive models are also required at different charging and discharging stages. Therefore, it is necessary to establish a model and use the actual measurement data and the IMM to estimate the SOC of the lead-carbon battery.

Step 1: Input interaction, i.e., initialize or reinitialize the model conditions, and obtain the $\hat{\boldsymbol{X}}_j(g|g)$ and $\boldsymbol{P}_j(g|g)$ of the three UKF filter inputs at the current time of the model, as:

$$\begin{cases} \hat{\boldsymbol{X}}_j(g|g)=\sum_{i=1}^{m}u_{ij}(g)\hat{\boldsymbol{X}}_i(g) \\ \boldsymbol{P}_j(g|g)=\sum_{i=1}^{m}u_{ij}(g)\left\{\boldsymbol{P}_i(g|g)+\left[\hat{\boldsymbol{X}}_i(g|g)-\hat{\boldsymbol{X}}_j(g|g)\right]\left[\hat{\boldsymbol{X}}_i(g|g)-\hat{\boldsymbol{X}}_j(g|g)\right]^{\mathrm{T}}\right\} \\ u_{ij}(g)=\dfrac{\pi_{ij}u_i(g)}{u_i(g)} \\ u_i(g)=\sum_{i=1}^{m}\pi_{ij}u_i(g)\quad j=1,2,\cdots,m \end{cases} \tag{7}$$

where $\hat{\boldsymbol{X}}_j(g|g)$ is the mixed estimated value of model j at time g; $\hat{\boldsymbol{X}}_i(g)$ is the estimated value of model i at time g; π_{ij} is the probability of model j switching to model i; $\boldsymbol{P}_j(g|g)$ is the covariance matrix value at time g; $u_{ij}(g)$ is the mixed probability of model j switching to model i at time g; $u_{\mathrm{i}}(g)$ and $u_j(g)$ are the probability of model i and j at time g, respectively.

Step 2: Unscented Kalman filtering. The battery voltage, current, observation equation, $\hat{\boldsymbol{X}}_j(g|g)$, and $\boldsymbol{P}_j(g|g)$ are used as inputs for unscented Kalman filtering.

First, calculate σ point at time g as:

$$\begin{cases} \boldsymbol{X}_j^p(g|g)=\hat{\boldsymbol{X}}_j(g|g),p=0 \\ \boldsymbol{X}_j^p(g|g)=\hat{\boldsymbol{X}}_j(g|g)+\left(\sqrt{(n+\lambda)\boldsymbol{P}_j(g|g)}\right)_p, \\ \qquad p=1,\cdots,n \\ \boldsymbol{X}_j^p(g|g)=\hat{\boldsymbol{X}}_j(g|g)-\left(\sqrt{(n+\lambda)\boldsymbol{P}_j(g|g)}\right)_p, \\ \qquad p=n+1,\cdots,2n \end{cases} \tag{8}$$

where $\boldsymbol{X}_j^p(g|g)$ is the estimated value of the p-th point in model j at time g.

The weights of expectation and variance, and the update of $\hat{\boldsymbol{X}}(g+1|g)$ and $\boldsymbol{P}(g+1|g)$ are calculated as:

$$\begin{cases} W_m^0=\dfrac{\lambda}{n+\lambda} \\ W_c^0=\dfrac{\lambda}{n+\lambda}+1-\alpha^2+\beta \\ W_m^p=W_c^p=\dfrac{1}{2(n+\lambda)},p=1,\cdots,2n \end{cases} \tag{9}$$

$$\begin{cases} \boldsymbol{X}^{(p)}(g+1|\ g)=\boldsymbol{A}(g)\boldsymbol{X}^{(i)}(g+1|\ g)+\boldsymbol{B}(g)u(g) \\ \hat{\boldsymbol{X}}(g+1|\ g)=\sum_{i=0}^{2n}W_m^p\boldsymbol{X}^{(p)}(g+1|\ g) \\ \boldsymbol{P}(g+1|\ g)=\sum_{i=0}^{2n}W_m^p\left[\hat{\boldsymbol{X}}(g+1|\ g)-\boldsymbol{X}^{(p)}(g+1|\ g)\right]\times \\ \qquad\qquad \left[\hat{\boldsymbol{X}}(g+1|\ g)-\boldsymbol{X}^{(p)}(g+1|\ g)\right]^{\mathrm{T}}+\boldsymbol{Q}(g) \end{cases} \tag{10}$$

where W is the corresponding weights of Sigma points; m is the mean; c is the covariance; the superscript of W represents the number of sampled points; α and β are the selected parameters; $\boldsymbol{A}$ and $\boldsymbol{B}$ are coefficient matrices; and $\boldsymbol{Q}$ is the noise variance matrix.

The updated σ at time $(g+1)$ are used to update $\hat{\boldsymbol{X}}(g+1|\ g)$ and $\boldsymbol{P}(g+1|\ g)$. The further prediction of the points is shown as:

$$\begin{cases} \boldsymbol{X}^p(g+1|g)=\hat{\boldsymbol{X}}(g+1|g),p=0 \\ \boldsymbol{X}^p(g+1|g)=\hat{\boldsymbol{X}}(g+1|g)+\left(\sqrt{(n+\lambda)\boldsymbol{P}(g+1|\ g)}\right)_p, \\ \qquad p=1,\cdots,n \\ \boldsymbol{X}^p(g+1|g)=\hat{\boldsymbol{X}}(g+1|g)-\left(\sqrt{(n+\lambda)\boldsymbol{P}(g+1|\ g)}\right)_p, \\ \qquad p=n+1,\cdots,2n \end{cases} \tag{11}$$

The above predicted points are weighed to calculate the mean and covariance matrix as:

$$\begin{cases} \boldsymbol{P}_{(XZ)}(g+1)=\sum_{P=0}^{2n} W_c^p\left[\boldsymbol{X}^p(g+1\mid g)-\hat{\boldsymbol{X}}(g+1\mid g)\right] \\ \qquad\qquad \left[Z^p(g+1\mid g)-\hat{Z}(g+1\mid g)\right]^{\mathrm{T}} \\ \boldsymbol{P}_{(ZZ)}(g+1)=\sum_{P=0}^{2n} W_c^p\left[Z^p(g+1\mid g)-\hat{Z}(g+1\mid g)\right] \\ \qquad\qquad \left[Z^p(g+1\mid g)-\hat{Z}(g+1\mid g)\right]^{\mathrm{T}}+R_g \end{cases} \tag{12}$$

where

$$\begin{cases} Z^P(g+1\mid g)=\boldsymbol{C}(g)\boldsymbol{X}^P(g+1\mid g)+\boldsymbol{D}(g)u(g)+\boldsymbol{V}(g) \\ \hat{Z}(g+1\mid g)=\sum_{P=0}^{2n} W_m^P Z^P(g+1\mid g) \end{cases} \tag{13}$$

where $\boldsymbol{C}$ and $\boldsymbol{D}$ are coefficient matrices; $\boldsymbol{V}$ is the observation noise; $u(g)$ is the voltage value at time g; Z is the systematic observation; and R is the observation of noise variance.

The calculations of the unscented Kalman gain, state update, and covariance update at time $(g+1)$ are:

$$\begin{cases} K_j(g+1)=\boldsymbol{P}_{(XZ)}(g+1\mid g)\boldsymbol{P}_{(ZZ)}^{-1}(g+1\mid g) \\ \hat{\boldsymbol{X}}_j(g+1)=\hat{\boldsymbol{X}}(g+1\mid g)+K_j(g+1)\times \\ \qquad [Z^P(g+1\mid g)-\hat{Z}(g+1\mid g)] \\ \boldsymbol{P}_j(g+1)=\boldsymbol{P}_j(g+1\mid g)-K_j(g+1)\times \\ \qquad \boldsymbol{P}_{(XZ)}(g+1\mid g)K_j^{\mathrm{T}}(g+1) \end{cases} \tag{14}$$

Step 3: Model probability update

The likelihood function of the jth model Λ_j can be expressed as:

$$\Lambda_j(g+1)=\frac{1}{(2\pi)^{\frac{n}{2}}\left|S_j(g+1)\right|^{\frac{1}{2}}}\times \exp\left(-\frac{1}{2}\nu_j^{\mathrm{T}}(g+1)S_j^{-1}(g+1)\nu_j(g+1)\right) \tag{15}$$

The residual ν_j and covariance S_j are respectively:

$$\nu_j(g+1)=Z(g+1)-H(g+1)\hat{\boldsymbol{X}}_j(g+1\mid g) \tag{16}$$

$$S_j(g+1)=H(g+1)\boldsymbol{P}_j(g+1)H^{\mathrm{T}}(g+1)+R(g+1) \tag{17}$$

where $H(g+1)$ is the first derivative of $Z(g+1)$.

The expression to calculate the mixed probability at the time $(g+1)$ is given by:

$$u_j(g+1)=\frac{\Lambda(g+1)u_j(g)}{C(g+1)} \tag{18}$$

where C is the normalization constant:

$$C(g+1)=\sum_{j=1}^{m}\Lambda_j(g+1)u_j(g+1) \tag{19}$$

Step 4: Output interaction

The model is fused with its corresponding probability to calculate the state estimation and covariance at the time $(g+1)$, as:

$$\hat{\boldsymbol{X}}(g+1)=\sum_{j=1}^{m}\hat{\boldsymbol{X}}(g+1)u_j(g+1) \tag{20}$$

$$\boldsymbol{P}(g+1)=\sum_{j=1}^{m}u_j(g+1)\left\{\boldsymbol{P}_j(g+1)+\left[[\hat{\boldsymbol{X}}_j(g+1)-\hat{\boldsymbol{X}}(g+1)][\hat{\boldsymbol{X}}_j(g+1)-\hat{\boldsymbol{X}}(g+1)]^{\mathrm{T}}\right]\right\} \tag{21}$$

Finally, the SOC is estimated jointly with the SOH as:

$$SOC(g+1)=SOH_{\min}\times\hat{\boldsymbol{X}}(g+1)\times\begin{bmatrix}1 & 0 & 0\end{bmatrix}^{\mathrm{T}} \tag{22}$$

where $SOH_{\min}$ represents the calculated value of SOH every 5 minutes; and $SOC(g+1)$ represents the estimated SOC value of interaction with SOH within a 5-minute period.

C. SOH Estimation Based on the Model and Measured Data

The battery SOH degrades as the diaphragm resistance increases. When energy storage batteries are used for frequency regulation, rapid charging and discharging are necessary. The internal chemical reactions of the battery are intense, and the diaphragm resistance changes significantly, resulting in significant fluctuations in SOH estimation. Therefore, the calculation period for the average diaphragm resistance in this paper is 5 min, and the sampling interval is 1 s. The diaphragm resistance R_{d1} is identified by the constant current charging interaction model and its model probability u_1 is denoted by R_{d11}, whereas the diaphragm resistance R_{d2} is identified by the constant voltage charging interaction model and its model probability u_2 is recorded as R_{d22}. The diaphragm resistance R_{d3} is identified by the dynamic discharge interaction model and its model probability u_3 is recorded as R_{d33}. Subsequently, the diaphragm resistances of the three models are combined, and represented as R_{now}, as shown in (23), while its average value is denoted as R_{ave} as shown in (24):

$$R_{\mathrm{now}}=R_{\mathrm{d1}}u_1+R_{\mathrm{d2}}u_2+R_{\mathrm{d3}}u_3 \tag{23}$$

$$R_{\mathrm{ave}}=\sum_{g=1}^{n}R_{\mathrm{now}}/n \tag{24}$$

The R_{ave} calculation period is 5 min and sampling interval is 1 s, with $n=300$. The mean values of the diaphragm and contact resistances in SOC estimation are used to estimate SOH, as:

$$SOH_{\min}=\frac{R_{\mathrm{eol}}-(R_{\mathrm{ave}}+R_{\mathrm{j}})}{R_{\mathrm{eol}}-R_{\mathrm{new}}}\times 100\% \tag{25}$$

where R_{eol} is the internal resistance when the battery reaches the end of its service life; and R_{new} is the internal resistance of the new battery.

V. Verification and Application of Measured Data

The measured data are used to validate and demonstrate the accuracy of the proposed method. Then, they are applied to the energy storage system to carry out real-time online SOC and SOH collaborative estimation of the lead-carbon battery.

A. Verification of actual measurement data

1) Lead-carbon Battery SOC Estimation

Figure 6 shows the lead-carbon battery experimental test platform. Its rated capacity, rated voltage, discharge cut-off voltage, the maximum charging current and the current battery SOH are 660 Ah, 2 V, 1.8 V, 600 A, and 95%, respectively. When discharging to 1.8 V, the SOC is regarded as 0, whereas when charging to 2.35 V, the SOC is regarded as 100%.

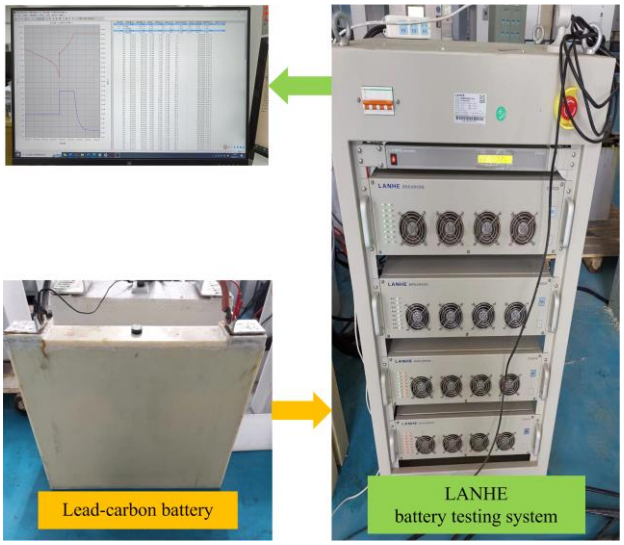

Fig. 6. Field test process.

The constant current discharge of the fully charged battery is conducted at 0.05 C or 33 A until the voltage is 1.95 V, and then the discharging stops. Voltage and current data are collected by the LANHE battery testing system, and the DS18B20 adhesive temperature sensor is used for temperature measurement. The ambient temperature is 25 ℃. During charging and discharging, the battery's temperature will rise slightly. However, the temperature rise only fluctuates within 3 ℃, so a constant test temperature of 25 ℃ can be considered.

The current and voltage during constant current charging are shown in Fig. 7(a). As seen, the current is constant at 66 A, while the voltage gradually increases from 1.8 V to 2.35 V. The voltage and current during constant voltage charging are shown in Fig. 7(b). The battery is considered to be fully charged when its voltage remains constant at 2.35 V and its current decreases gradually from 66 A to 9 A, as shown in Fig. 7(b). The voltage and current during constant current discharging are shown in Fig. 7(c). As seen, the current is constant at −33 A, and the voltage drops gradually from 2.35 V to 1.95 V at the end of the discharge.

The parameters of the established models of constant current charging interaction, constant voltage charging interaction and dynamic discharge interaction are identified based on the hysteresis characteristics, as shown in Figs. 8, 9, and 10, respectively.

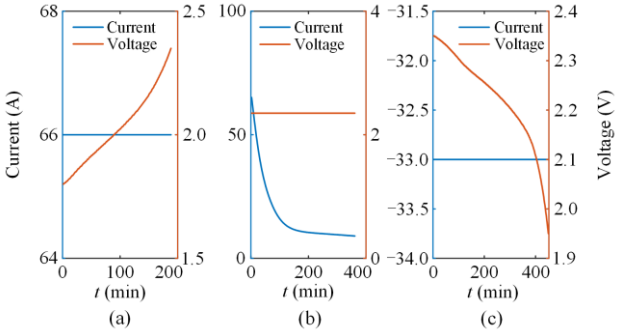

Fig. 7. Actual measured voltage and current curve. (a) Constant current charging. (b) Constant voltage charging. (c) Constant current discharging.

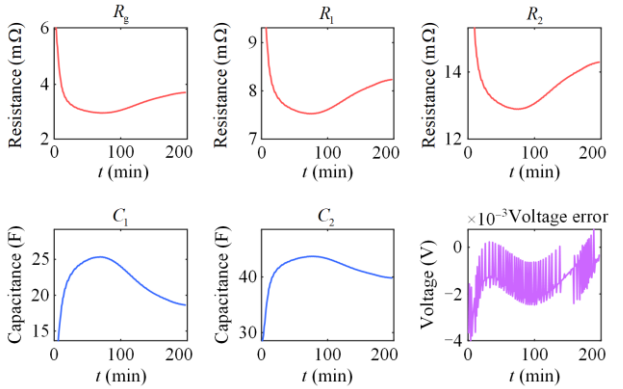

Fig. 8. Parameter identification results of the constant current charging interaction model.

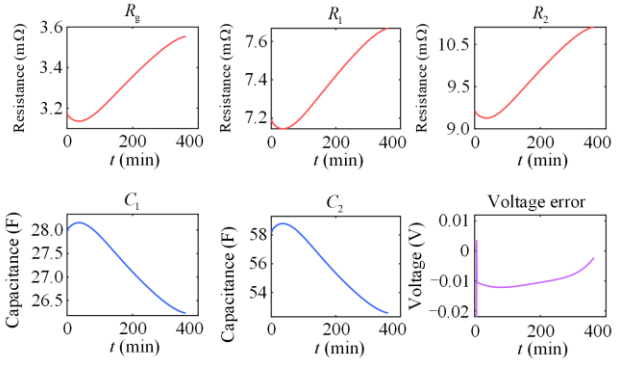

Fig. 9. Parameter identification results of the constant voltage charging interaction model.

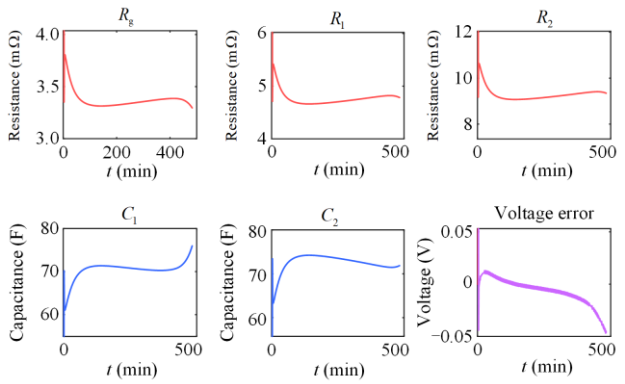

Fig. 10. Parameter identification results of the dynamic discharge interaction model.

By comparing Figs. 8, 9, and 10, it can be seen that R_d, R_1, R_2, C_1, and C_2 are different at each stage of constant current and constant voltage charging and discharging. The value of R_d identified by the three models is close to within 3.484 mΩ of the actual measured battery diaphragm resistance. The battery voltage errors between the measured and model voltages are within ±0.05 V, demonstrating the high accuracy of the parameter estimation of the three models.

The three models are fused interactively using the interactive multi-model algorithm to calculate the SOC of battery fusion. The SOC and its error are shown in Fig. 11 after coordination with the battery health status. As shown, the error of using the interactive multi-model algorithm to estimate the SOC of battery charge and discharge is within 2%, compared to the error of higher than 2% using the ampere-hour integration method.

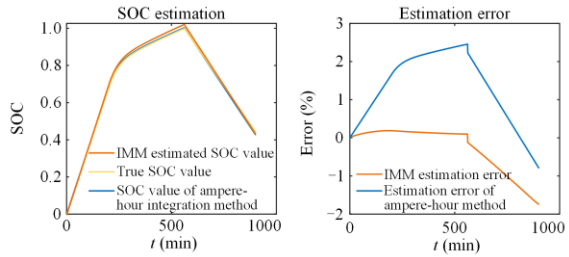

Fig. 11. Coordinated SOC estimation and its error.

2) Comparative Analysis of SOC Estimation for Different Equivalent Circuit Models

To verify the accuracy of SOC estimation in the equivalent circuit model proposed in this paper, a first-order and a traditional second-order RC equivalent circuit model are developed, and compared to the proposed model. Interactive multiple-model algorithms are used for SOC estimation, as shown in Fig. 12.

The SOC estimation errors of the first-order RC equivalent circuit model and the traditional second-order RC equivalent circuit model exceed 4% and 3%, respectively. In comparison, the error of SOC estimation using the proposed model is less than 2%, demonstrating higher SOC estimation accuracy when using the proposed model.

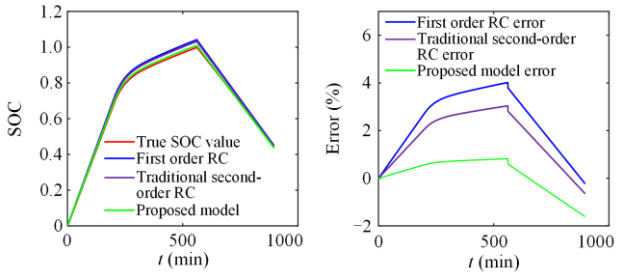

Fig. 12. SOC estimation results and errors of different equivalent circuit models.

3) SOH Estimation of Lead-carbon Battery

According to (23) and (24), the average value of the diaphragm resistance can be calculated, as shown in Fig. 13. As seen, the average value of diaphragm resistance is initially 3.9 mΩ, and is then stabilized at 3.5 mΩ.

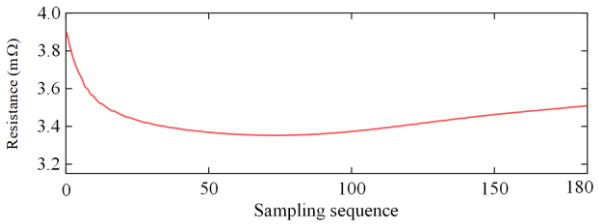

Fig. 13. Average value of diaphragm resistance.

When the battery reaches the end of its service life, the internal resistance R_{eol} is 8.32 mΩ, compared to the internal resistance R_{new} of the new battery of 4.656 mΩ. According to (25), the average SOH value during the charging and discharging test process is 94.84%, which is only 0.16% lower than the actual value of 95%. Thus, the estimation of SOH is very precise.

4) Applicability of SOH Estimation at Different Temperatures

To verify the applicability of the proposed SOH estimation algorithm at different temperatures, 2 V/660 Ah lead-carbon batteries with a 95% SOH at room temperature (25 ℃) are used. Charging and discharging experiments at temperatures of −20 ℃, 0 ℃, 25 ℃, and 45℃ are performed, and the voltage, current, and discharge capacity are recorded. The SOH is calculated based on the discharge capacity and Nameplate capacity as the reference value of SOH. Using the algorithm presented in this paper for calculating the mean value of the diaphragm resistance and estimating SOH, the estimation error of SOH is calculated (SOH from the proposed algorithm subtracts the estimated SOH based on the discharge amount from the estimated SOH value), and the results are presented in Table I.

TABLE I
COMPARISON OF SOH ESTIMATION AT DIFFERENT TEMPERATURES

Temperature (℃)	Discharge capacity (Ah)	Average value of diaphragm resistance (mΩ)	Reference value for SOH (%)	Estimated value of SOH (%)	Estimation error of SOH (%)
−20	333	5.276	50.45	45.96	−4.49
0	584	3.798	88.48	86.23	−2.18
25	627	3.485	95.00	94.84	−0.16
45	635	3.396	96.21	97.27	1.06

At temperatures of −20 ℃, 0 ℃, 25 ℃, and 45 ℃, the average membrane resistances estimated using the proposed algorithm are 5.276 mΩ, 3.798 mΩ, 3.485 mΩ, and 3.396 mΩ, respectively. The SOH are estimated to be 45.96%, 86.30%, 94.84%, and 97.27%, respectively. The discharged electricity at the four temperatures is 333 Ah, 584 Ah, 627 Ah, and 635 Ah, respectively. According to the discharge and Nameplate capacities, the SOH is 50.45%, 88.48%, 95%, and 96.21%, respectively. The estimation errors of the proposed algorithm are −4.49%, −2.18%, −0.16%, and 1.06%, respectively. The algorithm proposed here has small estimation errors and is still applicable at different temperatures.

B. Application

A high-proportion new energy power system model is built in the RTLAB environment for the application of this method, as shown in Fig. 14. The main components of the real-time simulation platform are the multi-core CPU, multi-FPGA expansion, and development host. Among them, the CPU is the main calculation unit for the large-scale new energy model and the IEEE 9-node model, and is also responsible for CAN, serial, TCP/IP, and IEC61850 communications, and other different communication implementations. FPGA is high-speed, and is responsible for some high-precision model calculations, high-speed IO, and optical fiber communication management. The CPU and FPGA use a high-speed PCIe bus for real-time communication.

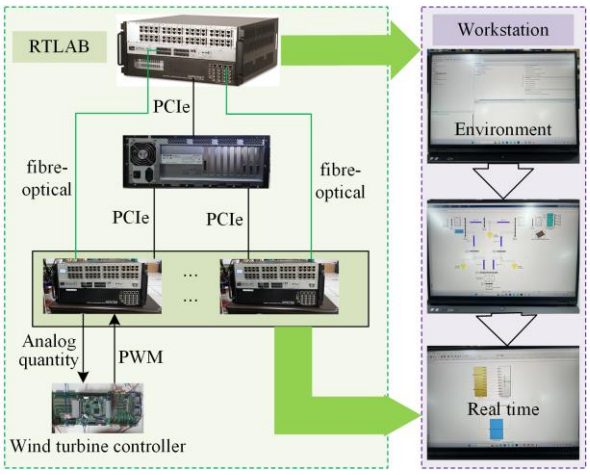

Fig. 14. Establishment of RTLAB real-time simulation environment.

A high-proportion new energy power system topology is shown in Fig. 15. The total capacity of the wind turbines is 200 MW, with a rated voltage of 690 V. The system is connected to the power grid through a transformer that boosts the voltage to 35 kV. The energy storage configuration is equipped with a lead-carbon battery of 20 MW/40 MWh, with a rated voltage of 690 V, and is also connected to the 35 kV power grid through a step-up transformer. The total capacity of the hydro turbine generator units is 400 MW, with rated voltage of 6.3 kV and step-up transformers connecting to the 35 kV power grid.

The energy storage configuration adopts a 2 V/660 Ah lead-carbon battery with a rated power of 660 W. A pack is comprised of 23 individual batteries, and 15 packs are connected in series to form a battery cluster. The voltage of the battery cluster is 690 V, with a total of 88 clusters. Each of the 22 clusters is boosted to 1500 V through a DC/DC converter and the 22 clusters are connected in parallel to a 5 MW PCS to form an independent energy storage unit. Each energy storage unit is connected to the power grid through a 1 kV/5 kV transformer, and four energy storage units form a 20 MW/40 MWh energy storage system. When simulating system frequency modulation, the voltage, current, and temperature of each battery can be measured.

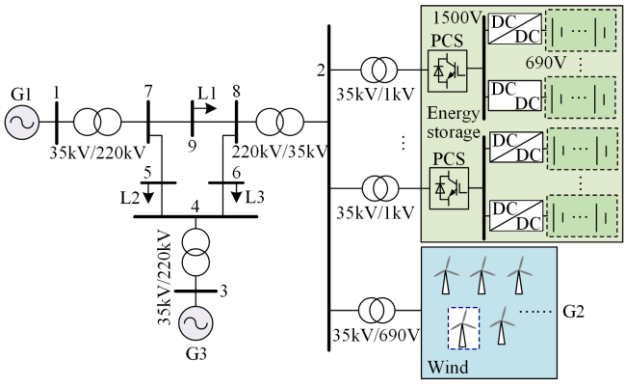

Fig. 15. High proportion new energy system topology.

The model consists of wind power, energy storage, and water turbine units, with detailed parameters shown in Table II.

A continuous load disturbance with an amplitude per unit value of 0.025 is added to the model. The SOC0 and the simulation duration are set to 60% and 25 min, respectively. In the condition of a continuous load disturbance, constant current charging is used when the

battery voltage is less than 2.35 V. Otherwise, constant voltage charging is used. During discharge, dynamic discharge is performed based on the actual demand for discharge. The voltage and current curves of the energy storage battery are shown in Figs. 16 and 17, respectively.

TABLE II
MODEL PARAMETERS

	Parameter	value
hydro turbine	rated voltage (kV)	6.3
	rated capacity (MW)	18.75
	rated power (MW)	15
	Total quantity (unit)	27
wind turbine	rated voltage (V)	690
	rated power (MW)	3
	Total quantity (unit)	67
Energy storage	Single battery voltage (V)	2
	Single battery capacity (Ah)	660
	Pack rated voltage (V)	690
	Pack rated power (kW)	227.7
	Battery cluster	88
	Energy storage unit	4
	PCS power (MW)	5

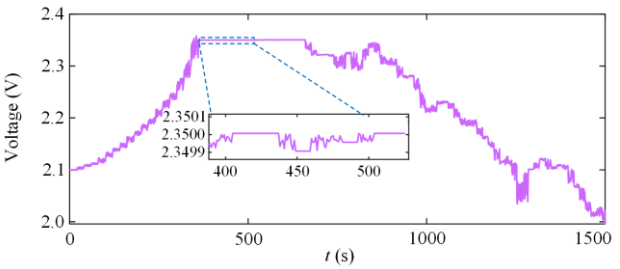

Fig. 16. Voltage curve of energy storage battery.

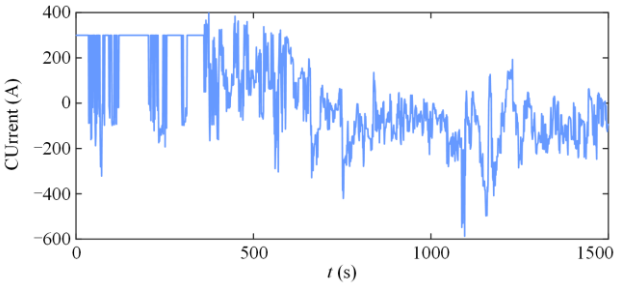

Fig. 17. Current curve of the energy storage battery.

In Fig. 16, it can be seen that the battery voltage rises gradually at first, and after reaching 2.35 V, it turns to constant voltage. The enlarged graph reveals that the voltage remains constant during the constant voltage charging phase when the battery is in the charging state, but fluctuates dynamically during discharge.

The error between the battery voltage and model identification voltage is depicted in Fig. 18. As seen, the voltage error fluctuates within ±0.05 V. The error is small, which indicates that the model is accurate. The SOC of the energy storage battery is estimated using the method proposed in this paper, and the corresponding results are shown in Fig. 19. As seen, the proposed method can adapt effectively to the SOC estimation of the battery during frequency regulation.

The parameters of the three interactive models are identified independently. Table III shows the calculated average values of the diaphragm resistance R_{ave} with a 5-min sampling period according to (23) and (24), and the calculated SOH according to (25).

As is seen from Table III, the average values of the diaphragm resistance R_{ave} for five cycles are 3.397 mΩ, 3.428 mΩ, 3.522 mΩ, 3.53 mΩ, and 3.533 mΩ, respectively. The contact internal resistance is 1.36 mΩ, and the SOH of the energy storage batteries calculated using (25) are 97.24%, 96.4%, 93.83%, 93.61%, and 93.53%, respectively. The average value of the diaphragm resistance during the entire process is 3.482 mΩ, and the estimated average SOH of the energy storage battery is 94.92%, which is only 0.08% different from the actual value of 95%, demonstrating high SOH estimation accuracy.

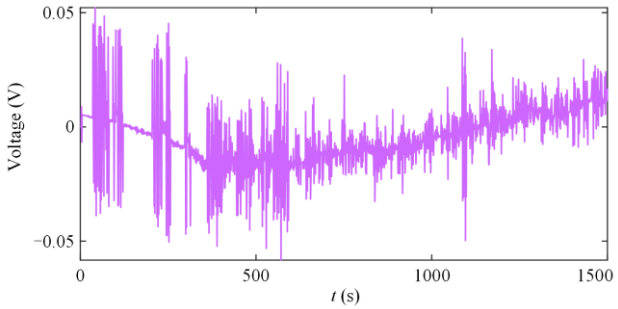

Fig. 18. Error diagram of battery voltage and model identification voltage.

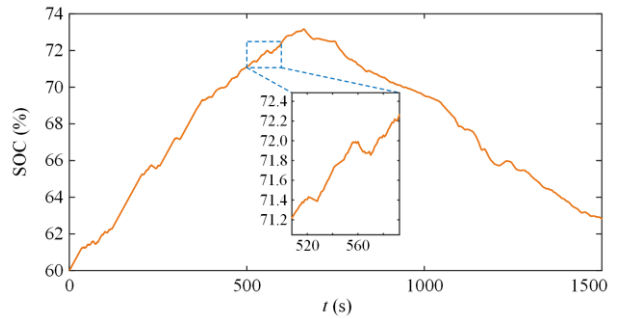

Fig. 19. SOC estimation of energy storage battery.

TABLE III
R_{AVE} AND SOH DURING FREQUENCY REGULATIONS

R_{ave} calculation cycle	R_{ave} (mΩ)	SOH (%)
1	3.397	97.24
2	3.428	96.40
3	3.522	93.83
4	3.530	93.61
5	3.533	93.53
Average value	3.482	94.92

VI. Conclusion

This paper proposes an online collaborative algorithm for estimating the SOC and SOH of lead-carbon batteries for frequency regulation in a power system with a high proportion of renewable energy. This algorithm mitigates the inaccuracies in the SOC and SOH estimations of energy storage batteries caused by constant charging and discharging on short time scales when the storage batteries participated in frequency regulation. The following conclusions can be drawn from the theoretical analysis, experimental data, and simulation results:

1) The composition materials of the resistance of lead-carbon batteries used for energy storage are different, and so are the time and magnitude of the changes in resistance values for different materials. Classifying the resistance values of batteries as contact and diaphragm resistances can clarify the physical meaning of the identified resistance values and provide a theoretical foundation for SOH estimation. Multiple experimental tests demonstrate that there are hysteresis characteristics during the charging and discharging process of lead-carbon batteries. Based on this, an equivalent circuit model of lead-carbon batteries is proposed that considers the contact and diaphragm resistances, and hysteresis characteristics.

2) The interactive multi-model algorithm with embedded unscented Kalman filter is used to perform SOC co-estimation on the established interactive models of constant current and voltage charging, and dynamic discharging. This algorithm is more suitable for estimating the SOC and SOH when energy storage lead-carbon batteries are charged and discharged alternately over short time scales. It is determined that the SOC estimation error is within 2% of that obtained using the measured data. This is less than the allowable standard error of 5%.

3) The interaction model is used to determine the diaphragm resistance which is multiplied by its model probability to obtain the mean for SOH estimation. Using the mean can reduce abnormal data errors. By validating the small estimation error of SOH through measured data at different temperatures, it demonstrates that the algorithm is applicable at different temperatures and is more in line with the actual application situation of energy storage batteries than other methods.

4) The estimation accuracy of the algorithm and its robustness are verified using the validation and application of the measured data.

Acknowledgment

Not applicable.

Authors' Contributions

Hongchun Shu: ideas, formulation of overarching research goals and aims. Wenlong Li: data curation, preparation of writing original draft. Guangxue Wang: methodology, and writing, reviewing and editing manuscript. Yiming Han: supervision, conducting a research and investigation process, and data collection. Jiannan Li: software and validation. Yutao Tang: visualization, and investigation. All authors read and approved the final manuscript.

Funding

This work is supported by the National Natural Science Foundation of China (52037003) and the Major Special and Technology Project of Yunnan Province (202002AF080001).

Availability of Data and Materials

Not applicable.

Declarations

Competing interests: The authors declare that they have no known competing financial interests or personal relationships that could have appeared to influence the work reported in this article.

Authors' Information

Hongchun Shu received his Ph.D. degree in electrical engineering from the Harbin Institute of Technology, China, in 1997. He became a professor in 1998 and completed his postdoctoral study from the Xi'an Jiao Tong University in 1999. He is currently among the famous teachers in the Yunnan Province, winning the first teaching merit of the Yunnan Province, the title of the national model teachers, the national excellent teachers, the National May 1 Labor Medal and the national excellent science and technology workers award. He presided over a total of 13 projects, including key and general projects of the National Natural Science Foundation of China, "863" projects of Yunnan province. He has more than 100 inventions as a first inventor, six books published by the state-level publishing press, 200 EI or SCI indexed papers, and one enterprise standard. He is currently a second-grade professor in China and a supervisor of Ph.D. students. His research interests include large-scale energy storage technology, fault location of distribution power system, protection and HVDC.

Wenlong Li received his B.Eng. degree from the Yunnan Minzu University, China in 2021. He is currently a M.Sc. student at the Kunming University of Science and Technology. His research interest covers new power systems and energy storage.

Guangxue Wang received the B.Eng. degree from the University of Jinan, China, in 2017. He is currently a Ph.D. student at the Kunming University of Science and Technology. His research interests include energy storage technology, renewable energy system control and HVDC transmission protection.

Yiming Han received the B.Eng. degree in Kunming City College, Kunming, China, in 2015, and received the Ph.D. degree from Kunming University of Science and Technology, Kunming, China in 2021. His research interests include power system protection and fault location, micro-grid automation, and renewable energy.

Jiannan Li received the B.Eng. degree in Qingdao University, China, in 2022. He is currently pursuing a master's degree at Kunming University of Technology. The main research direction is new power systems and energy storage.

Yutao Tang received the B.Eng. degree in Shandong Jianzhu University, Jinan, China, in 2018. He is currently working toward the Ph.D. degree with the Department of Electrical Engineering, Kunming University of Science and Technology, Kunming, China. His current research interests include the relay protection and control of power system with renewable energy.

REFERENCES

[1] J. Ouyang, J. Yu, and X. Long *et al.*, "Coordination control method to block cascading failure of a renewable generation power system under line dynamic security," *Protection and Control of Modern Power Systems*, vol. 8, no. 1, pp. 194-204, Mar. 2023.

[2] J. Wen, B. Zhou, and L. Wei, "Preliminary study on an energy storage grid for future power system in China," *Power System Protection and Control*, vol. 50, no. 7, pp. 1-10, Apr. 2022. (in Chinese)

[3] Z. Zhang and C. Kang. "Challenges and prospects for constructing the new-type power system towards a carbon neutrality future," *Proceedings of the CSEE*, vol. 42, no. 8, pp. 2806-2811, Apr. 2022. (in Chinese)

[4] H.S. Salama, G. Magdy, and A. Bakeer *et al*., "Adaptive coordination control strategy of renewable energy sources, hydrogen production unit, and fuel cell for frequency regulation of a hybrid distributed power system," *Protection and Control of Modern Power Systems*, vol. 7, no. 3, pp. 472-489, Sept. 2022.

[5] X. Zhou, Y. Liu, and J. Dai *et al.*, "Quantitative analysis of power system frequency characteristics considering wind power-energy storage-flexible HVDC transmission participation in frequency modulation," *Power System Protection and Control*, vol. 51, no. 6, pp. 30-44, Mar. 2023. (in Chinese)

[6] Y. Wang, M. Yang, and H. Xue *et al*., "Self-adaptive integrated control strategy of battery energy storage system considering SOC for primary frequency regulation," *Electric Power Automation Equipment*, vol. 41, no. 10, pp. 192-198+219, Oct. 2023. (in Chinese)

[7] J. Yang, T. Yang, and L. Luo *et al*., "Tracking-dispatch of a combined wind-storage system based on model predictive control and two-layer fuzzy control strategy," *Protection and Control of Modern Power Systems*, vol. 8, no. 4, pp. 974-989, Dec. 2023.

[8] Y. Guo, D. Yang, and Y. Zhang *et al*., "Online estimation of SOH for lithium-ion battery based on SSA-Elman neural network," *Protection and Control of Modern Power Systems*, vol. 7, no. 3, pp. 602-618, Sep. 2022.

[9] W. Yan, B. Zhang, and G. Zhao *et al*., "A battery management system with a lebesgue-sampling-based extended kalman filter," *IEEE Transactions on Industrial Electronics*, vol. 66, no. 4, pp. 3227-3236, Apr. 2019.

[10] X. Zhang, J. Hou, and Z. Wang *et al*., "Study of SOC estimation by the ampere-hour integral method with capacity correction based on LSTM," *Batteries-Basel*, vol. 8, no. 10, Oct. 2022.

[11] Y. Luo, P. Qi, and H. Huang *et al*., "Study on battery SOC estimation by ampere-hour integral method with capacity correction," *Automotive Engineering*, vol. 42, no. 5, pp. 681-687, May. 2020. (in Chinese)

[12] F. Tan, J. Zhao, and Q. Li. "Adaptive SOC estimation strategy for lithium battery based on simplified hysteresis OCV model," *Proceedings of the CSEE*, vol. 41, no. 2, pp. 703-714, Jan. 2021. (in Chinese)

[13] H. Liu, P. Zhou, and Z. Zhou *et al*., "Fast estimation of open circuit voltage for lithium-ion batteries," *Journal of Mechanical Engineering*, vol. 58, no. 8, pp. 227-235+243, Apr. 2022. (in Chinese)

[14] Z. Cui, L. Wang , and Q. Li *et al*., "A comprehensive review on the state of charge estimation for lithium-ion battery based on neural network," *International Journal of Energy Research*, vol. 46, no. 5, pp. 5423-5440, Apr. 2022.

[15] X. Mao , S. Song, and F. Ding, "Optimal BP neural network algorithm for dtate of charge estimation of lithium-ion battery using PSO with levy flight," *Journal of Energy Storage*, vol. 49, May. 2022.

[16] L. Mao, J. Wen, and J. Zhao *et al*., "Joint estimation of SOC and SOH at lithium-ion battery charging cut-off voltage based on an ensemble extreme learning machine," *Power System Protection and Control*, vol. 51, no. 11, pp. 86-95, Jun. 2023. (in Chinese)

[17] Y. Li, K. Li, and X. Liu *et al*., "A hybrid machine learning framework for joint SOC and SOH estimation of lithium-ion batteries assisted with fiber sensor measurements," *Applied Energy*, vol. 325, Nov. 2022.

[18] C. Jiang, S. Wang, and B. Wu *et al*., "A state-of-charge estimation method of the power lithium-ion battery in complex conditions based on adaptive square root extended kalman filter," *Energy*, vol. 219, Mar. 2021.

[19] S. Ji, Y. Sun, and Z. Chen *et al*., "A multi-scale time method for the state of charge and parameter estimation of lithium-ion batteries using MIUKF-EKF," *Frontiers in Energy Research*, vol. 10, Aug. 2022.

[20] M. Al-Gabalawy, N.S. Hosny, and J.A. Dawson *et al*., "state of charge estimation of a li-ion battery based on extended kalman filtering and sensor bias," *Interna-*

tional Journal of Energy Research, vol. 45, no. 5, pp. 6708-6726, Apr. 2021.

[21] G. Yan , H. Li, and S. Duan *et al*., "Energy storage battery state estimation based on model parameter identification," *Proceedings of the CSEE*, vol. 40, no. 44, pp. 8145-8154+8251, Sep. 2020. (in Chinese)

[22] Z. Wang, X. Tuo, and J. Zhou *et al*., "Performance study of large capacity industrial lead-carbon battery for energy storage," *Journal of Energy Storage*, vol. 55, Nov. 2022.

[23] O. Jhabli, M. Boutamart, and E. El Mouchtari *et al*., "New insights into carbonaceous materials and lead/carbon composites in lead-carbon battery," *Journal of Energy Storage*, vol. 56, Dec. 2022.

[24] X. Li, G. Geng, and Q. Jiang *et al*., "Case study of power allocation strategy for a grid-side lead-carbon battery energy storage system," *IET Renewable Power Generation*, vol. 16, pp. 435-446, Feb. 2022.

[25] X. Dong, X. Zhang, and J. Zhao *et al*., "Multi-maneuvering sources DOA tracking with improved interactive multi-model multi-bernoulli filter for acoustic vector sensor (AVS) array," *IEEE Transactions on Vehicular Technology*, vol. 70, no. 8, pp. 7825-7838, Aug. 2021.

[26] D. Chen, C. Wang, and Z. Zhu *et al*., "Lithium battery state-of-charge estimation based on interactive multi-model unscented kalman filter algorithm," *Energy Storage Science and Technology*, vol. 9, no. 1, pp. 257-265, Jan. 2020. (in Chinese)

[27] R. Zhu, B. Duan, and J. Zhang *et al*. "Co-estimation of model parameters and state-of-charge for lithium-ion batteries with recursive restricted total least squares and unscented kalman filter," *Applied Energy*, vol. 277, Nov. 2020.